Electronic Supplementary Material (ESI) for Journal of Materials Chemistry A.

Electronic Supplementary Information

$NiCo_2O_4$ nanosheet as a novel oxygen-evolution-reaction cocatalyst in-situ bonded on g-C_3N_4 photocatalyst for excellent overall water splitting

Cheng Cheng[1], Liuhao Mao[1], Jinwen Shi*, Fei Xue, Shichao Zong, Botong Zheng, Liejin Guo

[1]These authors contributed equally to this work.

State Key Laboratory of Multiphase Flow in Power Engineering (MFPE), International Research Center for Renewable Energy (IRCRE), Xi'an Jiaotong University (XJTU), 28 West Xianning Road, Xi'an 710049, China.

jinwen_shi@mail.xjtu.edu.cn *Corresponding author.

Chemicals and materials

All reagents were analytical grade and used without further purification. Urea, cobalt chloride hexahydrate ($CoCl_2·6H_2O$), nickel chloride hexahydrate ($NiCl_2·6H_2O$), silver nitrate ($AgNO_3$), Triethanolamine (TEOA, $C_6H_{15}NO_3$) and hexamethylenetetramine (HMT, $C_6H_{12}N_4$) were purchased from Sinopharm Chemical Reagent Co., Ltd. chloroplatinic acid hexahydrate ($H_2PtCl_6·6H_2O$) and Nafion solution (D1020) were purchased from Alfa Aesar and Dupont, respectively. The $H_2PtCl_6·6H_2O$ was dissolved in deionized water to form an aqueous solution with the Pt content of 0.9005 mg mL^{-1}. The deionized water used in experiments was deionized water with the resistivity of 18.25 MΩ cm.

Preparation of photocatalysts

CN-10.00NiCoO was prepared by the similar procedure to except that the mass ratio of Co element to CN was adjusted to 10%. The intermediate without calcination in air was denoted as CN-10.00NiCoO-pre. After photocatalytic overall water splitting reaction, the photocatalyst was recycled by centrifugation and denoted as CN-1.00NiCoO-R.

Material characterization

X-ray diffraction (XRD) patterns were measured by a diffractometer (PANalytical X'pert MPD, Netherlands) operated at 40 kV and 40 mA with Ni-filtered Cu Kα irradiation (λ = 1.5406 Å). Fourier transform infrared spectra (FTIR) were measured on a FTIR spectrophotometer (Bruker Vertex70, Germany) by using the KBr pellet technique. Scanning electron microscopy (SEM) images were obtained on a field-emission scanning electron microscope (JEOL JSM-7800F, Japan). Transmission electron microscopy (TEM) and high-angle annular dark field-scanning TEM (HAADF-STEM) images were observed from a microscope (FEI Tecnai G^2 F30 S-Twin transmission electron, USA) with accelerating voltage of 300 kV. X-ray photoelectron spectra (XPS) were measured by a X-ray photoelectron spectroscope (Kratos Analytical Axis Ultra DLD, Japan) with a monochromatized Al Kα (hν = 1486.69 eV) line source (150 W). The C 1s peak at 284.8 eV was used as referenced to all the binding energies. UV–vis absorption spectra (UV–vis) were recorded on a spectrophotometer (Agilent Cary 5000, USA) with $BaSO_4$ as the reference and equipped with a diffuse-reflectance accessory. Photoluminescence spectra (PL) were obtained from a steady-state fluorescence spectrophotometer (PTI QuantaMaster 40, USA) at room temperature with an excitation wavelength of 337 nm. The light spectrum was recorded by a fiber optical spectrometer (Avantes avaspec-ULS2048XL-RS-EVO-UA, Netherlands).

(Photo)electrochemical measurement

(Photo)electrochemical measurement was carried out in a three-electrode chemical cell by using a CH Instruments CHI 760D scanning potentiostat. Pt foil and Ag/AgCl electrode were applied as the counter electrode and reference electrode, respectively, and N_2-saturated Na_2SO_4 aqueous solution (0.5 M) was employed as the electrolyte. To prepare the working electrodes for electrochemical measurements, the as-prepared photocatalyst (1 mg) was first ultrasonically dispersed in the mixture of deionized water (250 μL), ethanol (250 μL), and Nafion solution (10 μL, 10 wt%) for 1 h to form a homogeneous suspension, and then the above suspension (10 μL) was transferred onto a glassy carbon rotating disk electrode (RDE, CHI 104, 3 mm of diameter,) via a controlled drop casting approach. After the natural drying under ambient temperature, the resulting electrode was obtained to serve as the working electrode. The working electrodes for transient photocurrent measurement were prepared by following the same method but spreading the suspension (1 mL) onto a fluorine-doped tin oxide (FTO) glass plate (2×3 cm^2) instead of the glassy carbon RDE. Electrochemical impedance spectroscopy (EIS) curves were measured from 100 kHz to 0.1 Hz at an applied voltage of +1.0 V vs Ag/AgCl. Linear sweep voltammetry (LSV) curves were conducted at a scan rate of 10 mV/s. The measured potentials vs. Ag/AgCl were converted to reversible hydrogen electrode (RHE) scale via the Nernst equation. Transient photocurrent response (i-t) curves were recorded at an applied voltage of +0.6 V vs Ag/AgCl.

The measurement of apparent quantum yield (AQY) was carried out under the irradiation of Xe lamp (300 W) equipped with different band-pass filters (380, 405, 425, 440 and 480 nm; the corresponding

UV–vis spectra of different band-pass filters are shown in Fig. S9c-g). The intensity of irradiated light was recorded from a Netherlands Avantes AvaSpec-2048-USB2 spectroradiometer.

The AQY value was obtained by the following equation:

$$AQY(\%) = \frac{Number\ of\ reacted\ electrons}{Number\ of\ incident\ photons} \times 100\%$$

$$= \frac{Number\ of\ evolved\ H_2\ molecules\ \times\ 2}{Number\ of\ incident\ photons} \times 100\%$$

The turnover number (TON) value was obtained by the following equation:

$$TON = \frac{Total\ moles\ of\ product}{Moles\ of\ catalyst} = \frac{Total\ moles\ of\ H_2}{Moles\ of\ photocatalyst}$$

The light powers were 143 mW cm^{-2} and 127 mW cm^{-2} for full-arc and visible-light irradiation, respectively.

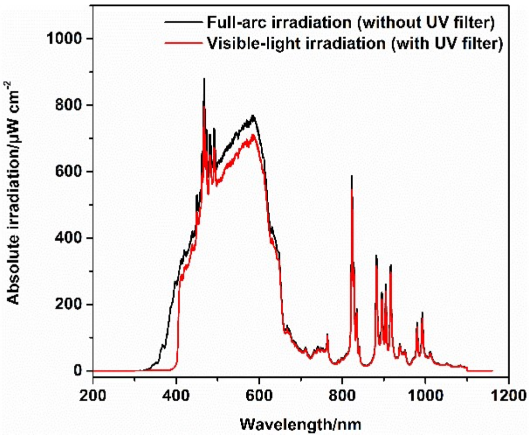

Figure S1. The spectrum of the incident light without or with UV filter**.**

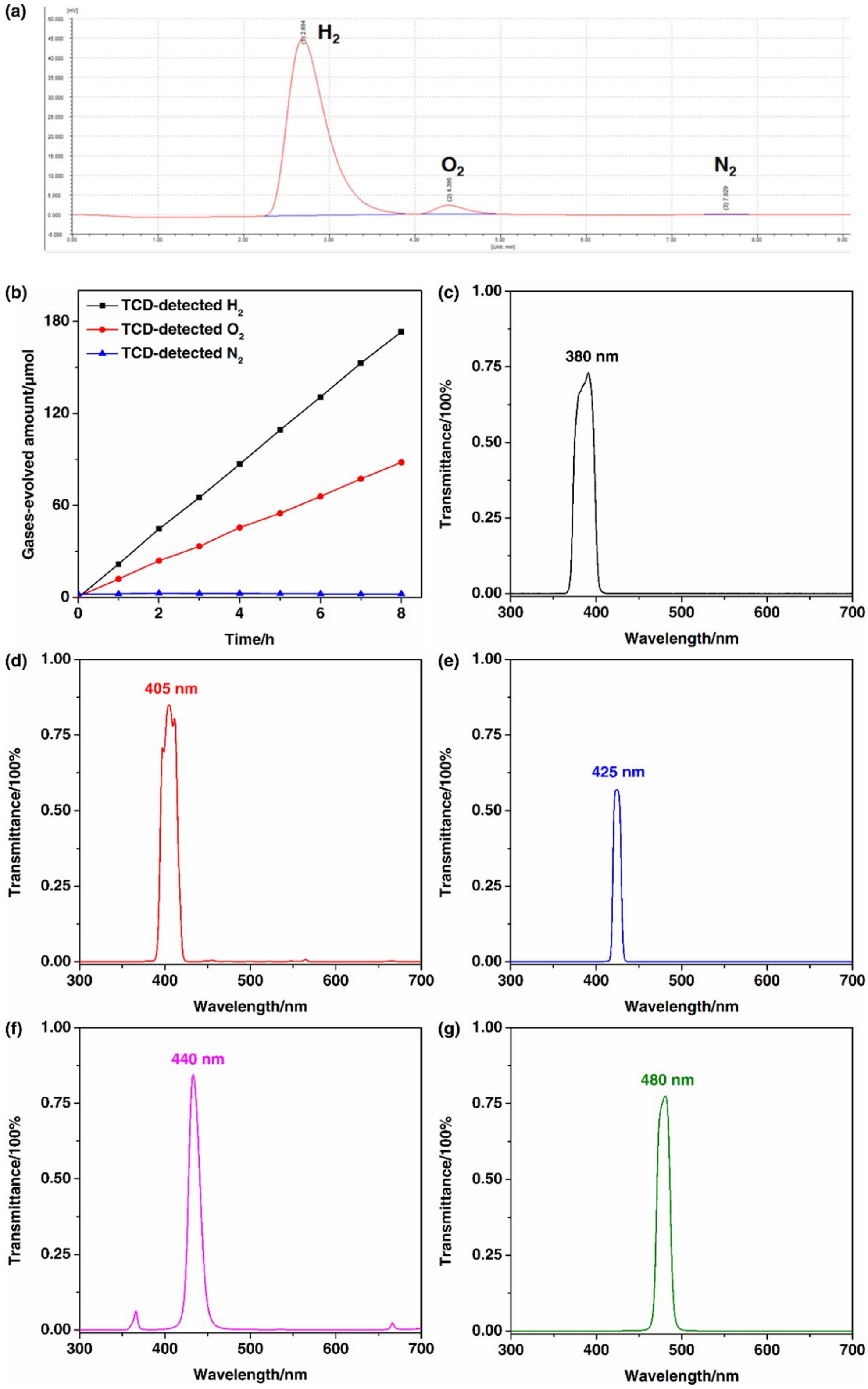

Figure S2. (a) A typical gas chromatograph trace picture of photocatalytic overall water splitting for H_2 and O_2 evolution. (b) Time courses of photocatalytic overall water splitting under full-arc irradiation over 3Pt-CN-1.00NiCoO. UV–vis spectra of different band-pass filters: (c) 380, (d) 405, (e) 425, (f) 440 and (g) 480 nm.

Typical (100) and (002) diffraction peaks of g-C_3N_4 were observed in CN-0.00NiCoO, CN-1.00NiCoO-pre and CN-1.00NiCoO, proving that the reflux and the thermal treatment had little influence on the structure of g-C_3N_4. The characteristic peaks of NiCoO-pre were attributed to the 4Ni(OH)$_2$·NiOOH (JCPDS No. 00-006-0044) and Co(OH)$_2$ (JCPDS No. 01-074-1057). In addition, the characteristic peaks of metal hydroxides could not be found in the CN-1.00NiCoO-pre since the low content and low crystallinity degree.

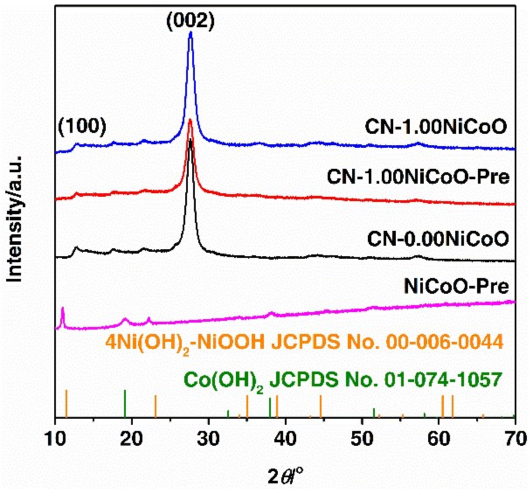

Figure S3. XRD patterns of NiCoO-pre, CN-0.00NiCoO, CN-1.00NiCoO-pre and CN-1.00NiCoO.

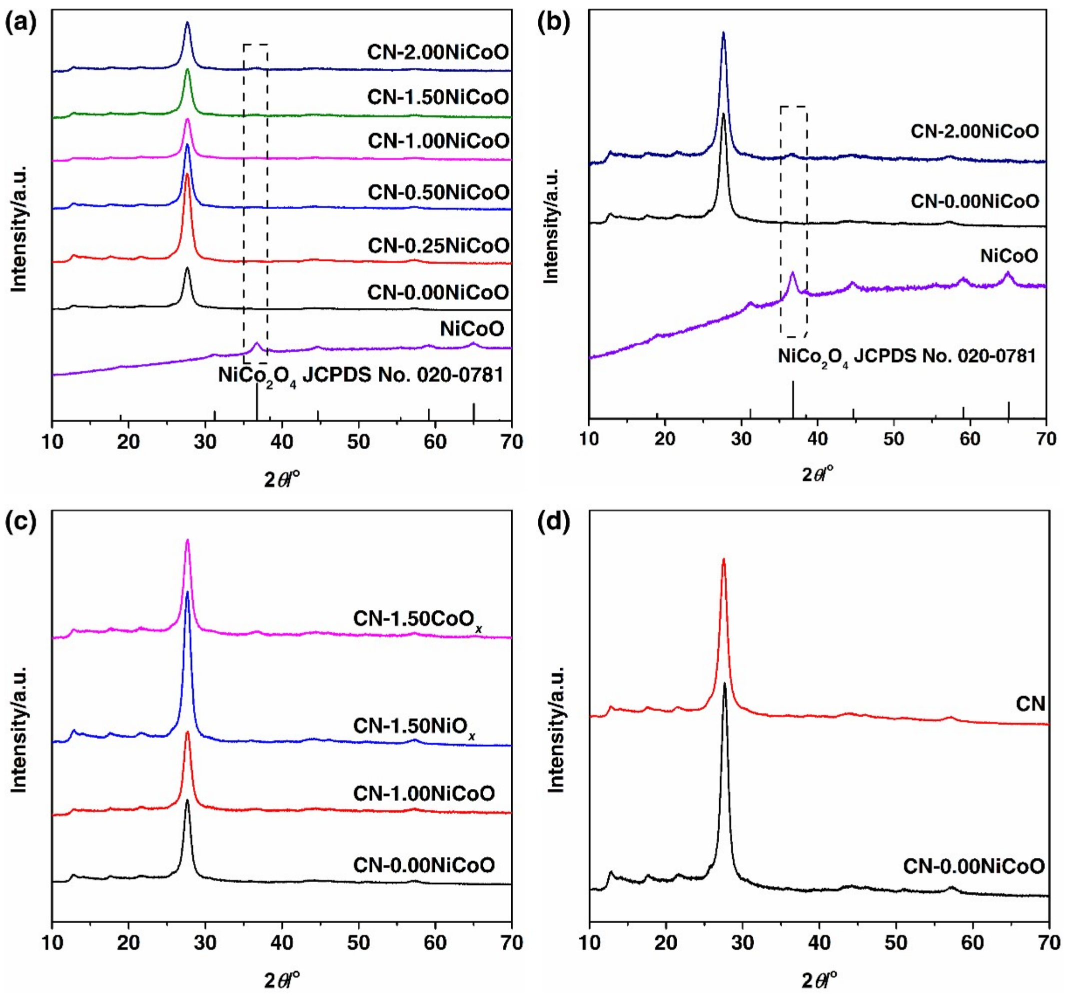

Figure S4. XRD patterns of (a) NiCoO, CN-*x*NiCoO (x = 0.00, 0.25, 0.50, 1.00, 1.50 and 2.00); (b) CN-0.00NiCoO, CN-2.00NiCoO and NiCoO;(c) CN-0.00NiCoO, CN-1.00NiCoO, CN-1.50NiO$_x$ and CN-1.50CoO$_x$, and (d) CN-0.00NiCoO and CN.

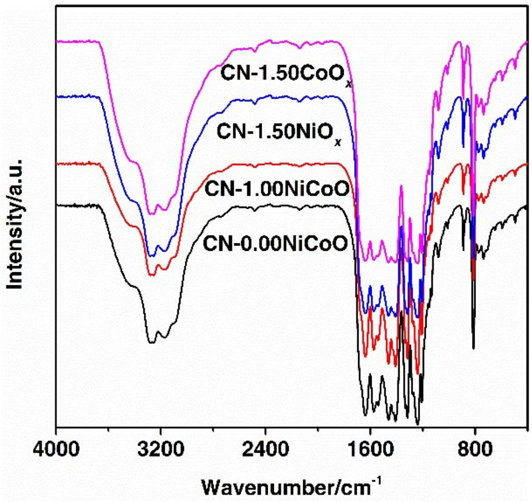

Figure S5. FTIR spectra of CN-0.00NiCoO, CN-1.00NiCoO, CN-1.50NiO$_x$ and CN-1.50CoO$_x$.

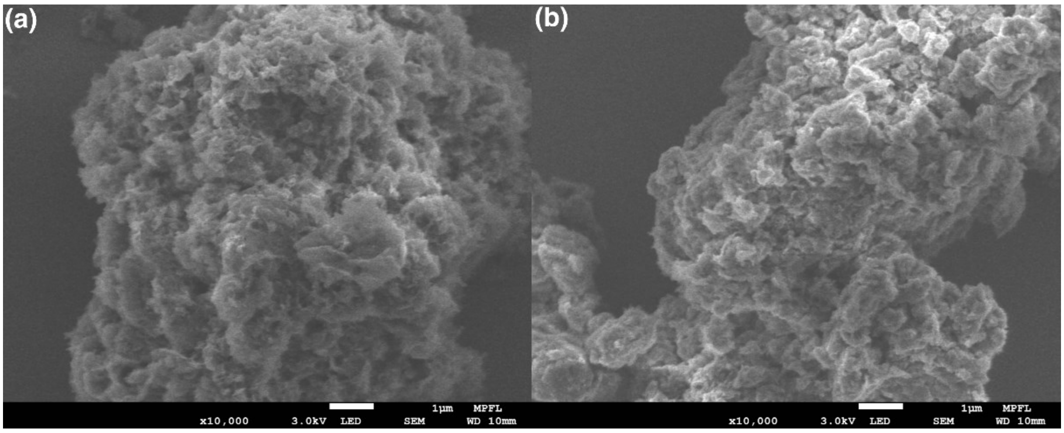

Figure S6. SEM images for (a) CN-0.00NiCoO and (b) CN-1.00NiCoO.

Fig. S7a shows CN-10.00NiCoO-pre had the diffraction peaks belonged to $Co(OH)_2$ and $Ni(OH)_2$ besides the diffraction peaks of g-C_3N_4. Fig. S7b shows CN-10.00NiCoO had the obvious diffraction peaks of NiCoO, the decrease of diffraction peaks intensities for g-C_3N_4 might be attributed by the relatively reduced content of CN and marked inhibition effect of NiCoO on the two-dimensional structure that induced diffraction reduction. The results demonstrated the process of immobilizing NiCoO on CN as described below. Co^{2+} and Ni^{2+} ions were first adhered to the surface of CN in the forms of hydroxides, then a calcination procedure was implemented to make NiCoO in-situ grow on CN for obtaining $NiCo_2O_4$/g-C_3N_4 coupled composite.

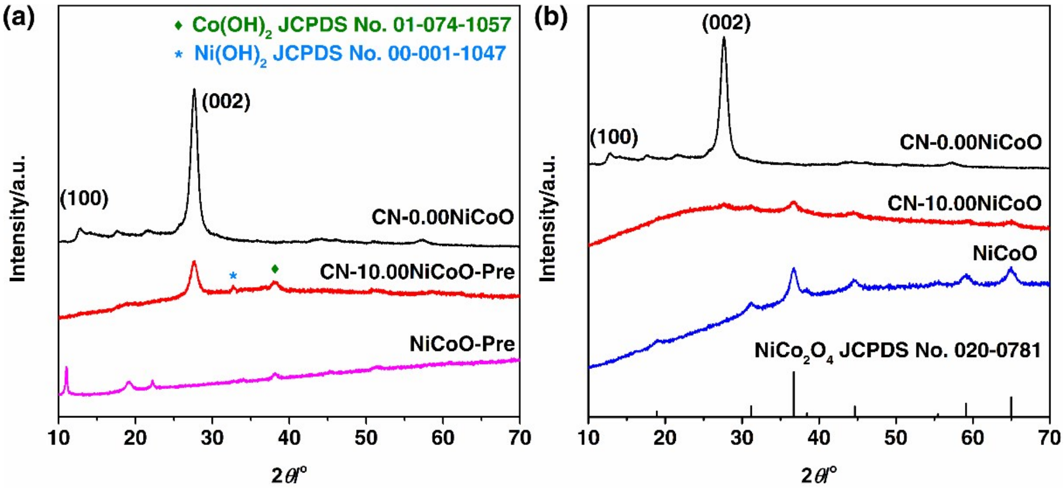

Figure S7. XRD patterns of (a) CN-0.00NiCoO, CN-10.00NiCoO-pre and NiCoO-pre; (b) CN-0.00NiCoO, CN-10.00NiCoO and NiCoO.

As seen in Fig. S8a and S8b, the NiCoO-pre possessed a hexagonal morphology with a length of side about 200-300 nm, and the bare NiCoO had a 2D sheet structure. The thickness and size were both increased after calcination in the air, which was attributed to the crystal growth at high temperature.

Pristine g-C_3N_4 was composed of aggregated nanosheets (Fig S8c and S8d), the surface of CN seemed to be less ordered and smooth. Fig. S8e and S8f present the SEM images of CN-10.00NiCoO, which were quite different from those of CN-0.00NiCoO. Some standing nanosheets grew on the surface of CN, in Fig. S8e and S8f, it could be obviously observed that the nanosheets of NiCoO were intimately anchored on CN. NiCoO nanosheets on CN nanosheet had sizes about hundreds of nanometers in diameters, which was dramatically smaller than that of bare NiCoO. Besides the supporting effort of CN nanosheet existed as substrates, this size reduction of NiCoO nanosheets on CN could be attributed to the fact that in the preparation process of CN-*x*NiCoO, a smaller amount of $NiCl_2 \cdot 6H_2O$ and $CoCl_2 \cdot 6H_2O$ was added. In Fig. S8g, it was observed that CN-10.00NiCoO-pre had similar structure to CN-10.00NiCoO, NiCoO-pre nanosheets were slantingly or vertically anchored on CN.

So, it could be deduced that CN-1.00NiCoO should have smaller and thinner NiCoO nanosheets compared with CN-10.00NiCoO because lesser amount of $NiCl_2 \cdot 6H_2O$ and $CoCl_2 \cdot 6H_2O$ was added in the preparation process. As it was supposed to be, the TEM and STEM images in Fig. 2 showed NiCoO nanosheets on CN nanosheet had sizes about dozens nanometers in diameters.

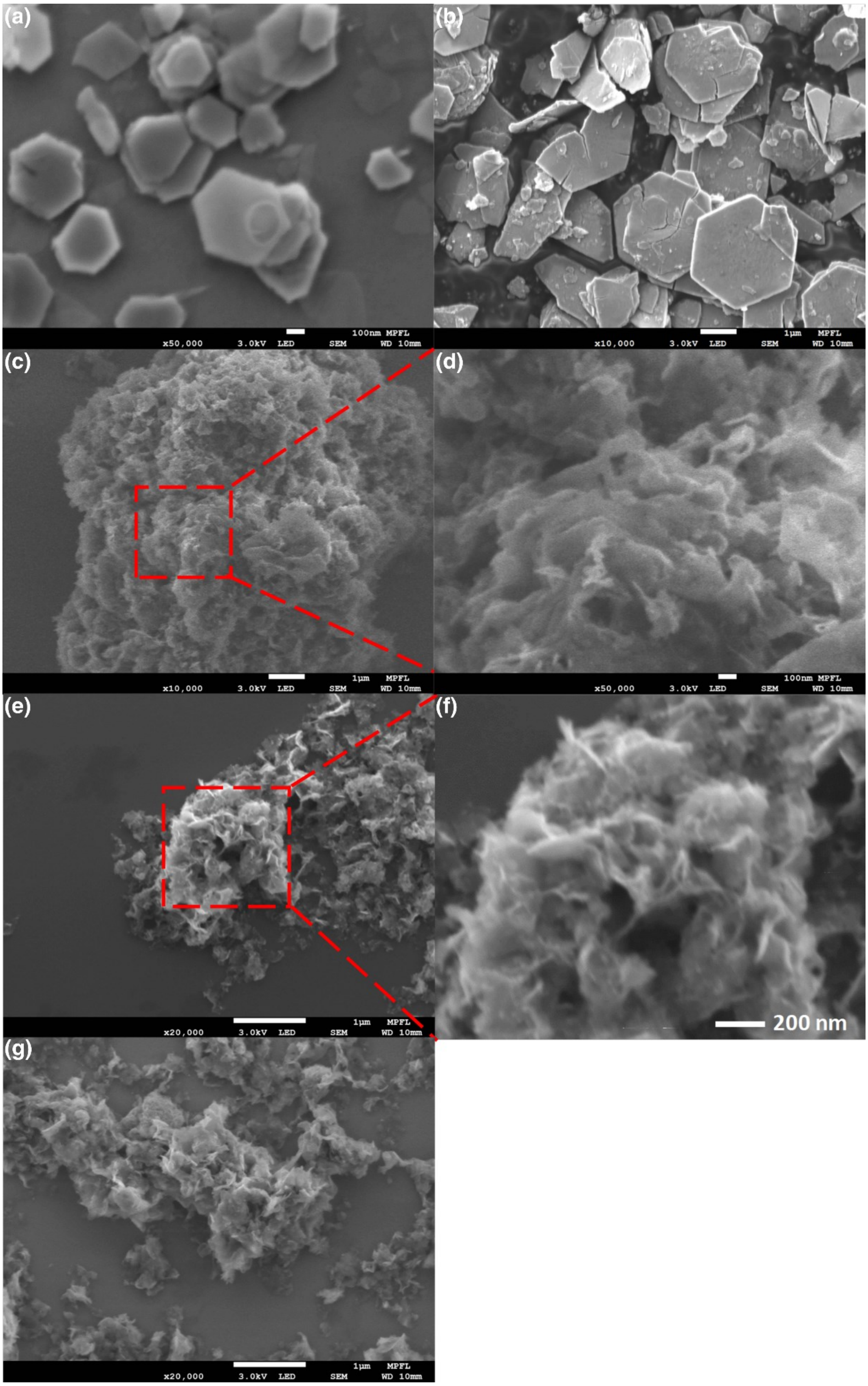

Figure S8. SEM images of (a) NiCoO-pre, (b) NiCoO, (c) and (d) CN-0.00NiCoO, (e) and (f) CN-10.00NiCoO, (g) CN-10.00NiCoO-pre, (d) and (f) were the magnifying images of red circles in (c) and (e), respectively.

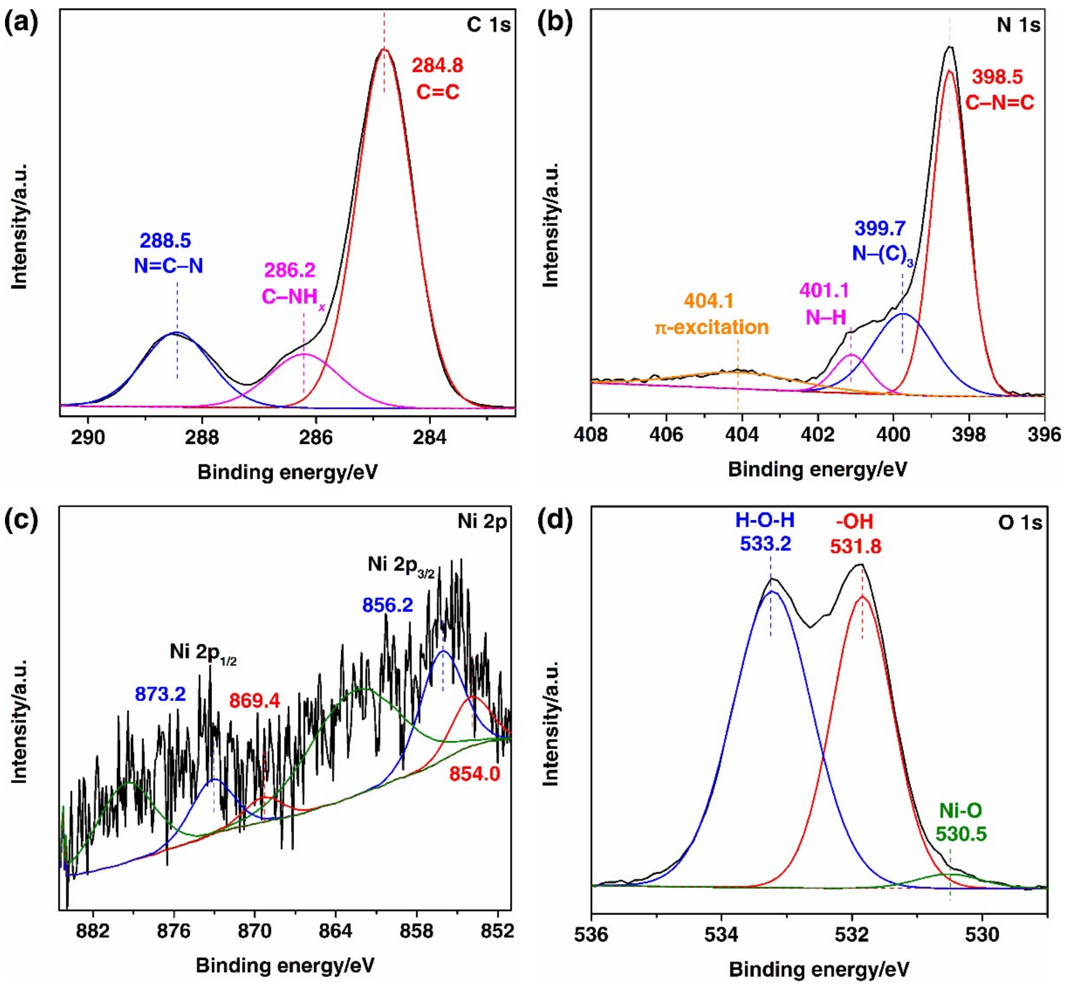

Figure S9. High-resolution XPS spectra of (a) C 1s, (b) N 1s, (c) Ni 2p and (d) O 1s for CN-1.50NiO$_x$.

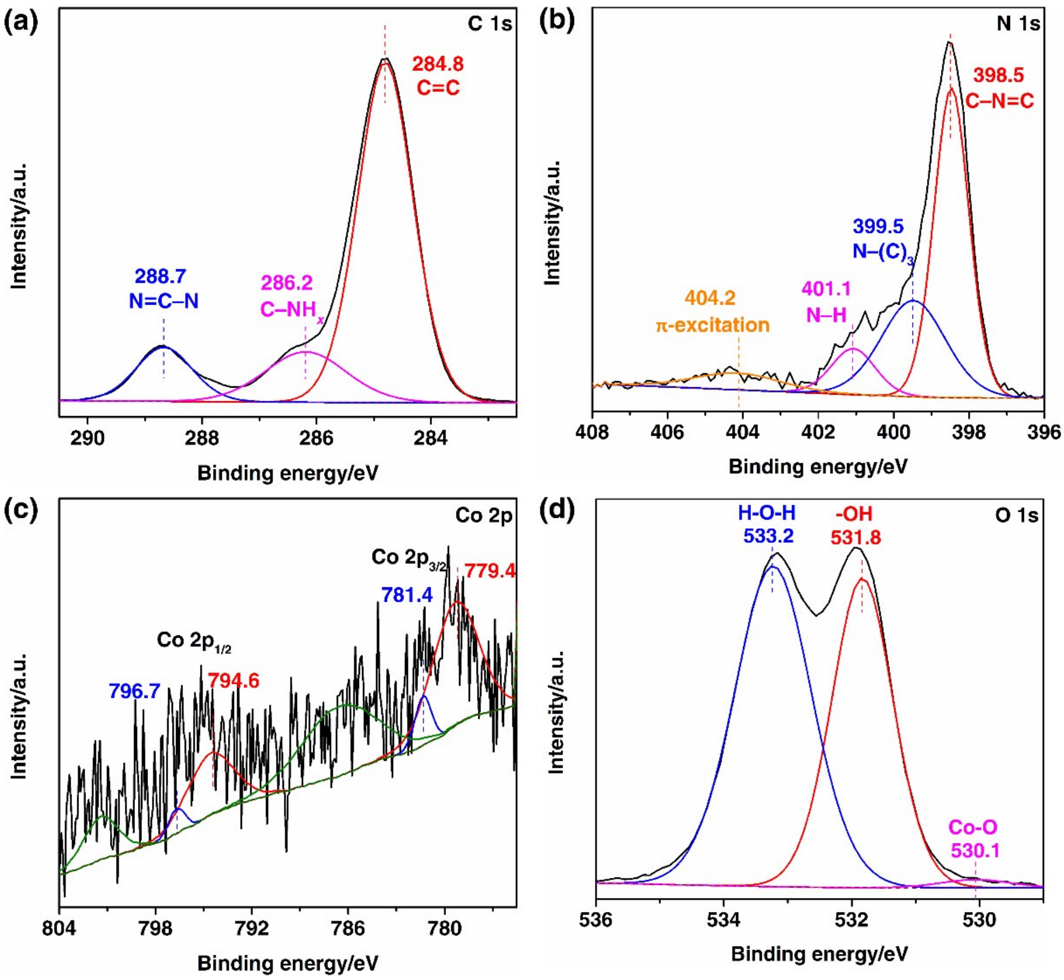

Figure S10. High-resolution XPS spectra of (a) C 1s, (b) N 1s, (c) Ni 2p and (d) O 1s for CN-1.50CoO$_x$.

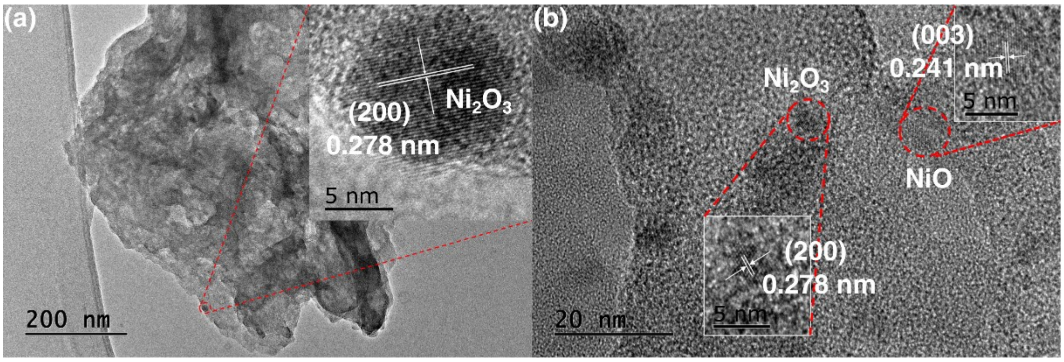

Figure S11. (a, b) TEM and HRTEM (inset) images of CN-1.50NiO$_x$.

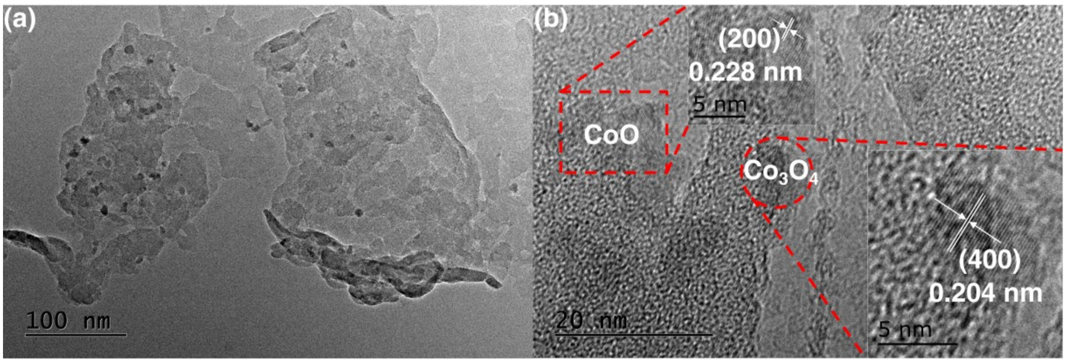

Figure S12. (a, b) TEM and HRTEM (inset) images of CN-1.50CoO$_x$.

Control experiments showed that no O_2 was produced in the absence of either photocatalyst or light irradiation, indicating that neither the photolysis of solution in the photocatalytic system nor the non-photocatalytic effect (e.g., mechano-catalysis) contributed to O_2 evolution.

The photocatalytic O_2-evolution rates of photocatalysts slowed down due to the Ag^+ was reduced to metallic Ag^0 and it deposited on the surface of photocatalysts, hindering the light absorption as well as decreasing the number of active sites for reaction.

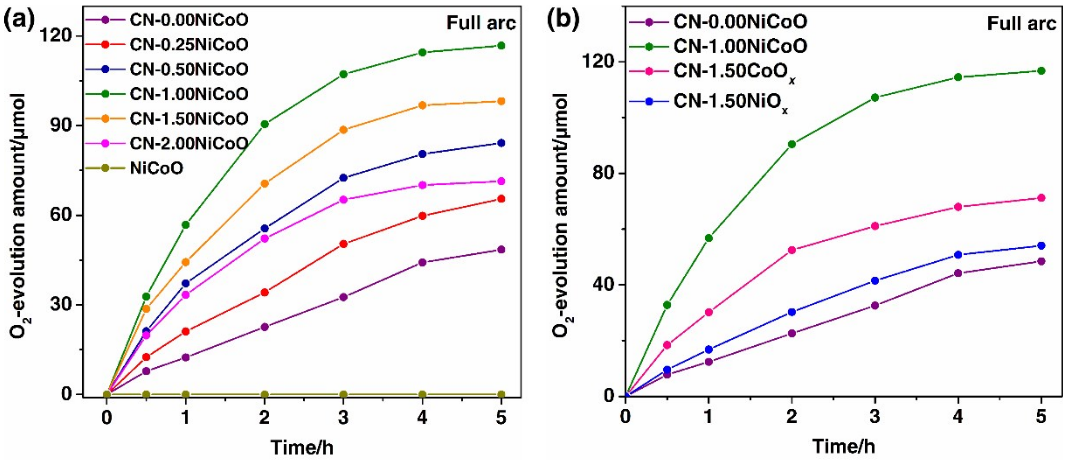

Figure S13. Time courses of photocatalytic O_2 evolution under full-arc irradiation over (a) CN-xNiCoO (x = 0.00, 0.25, 0.50, 1.00, 1.50 and 2.00) and NiCoO; (b) CN-0.00NiCoO, CN-1.00NiCoO, CN-1.50NiO_x and CN-1.50CoO_x.

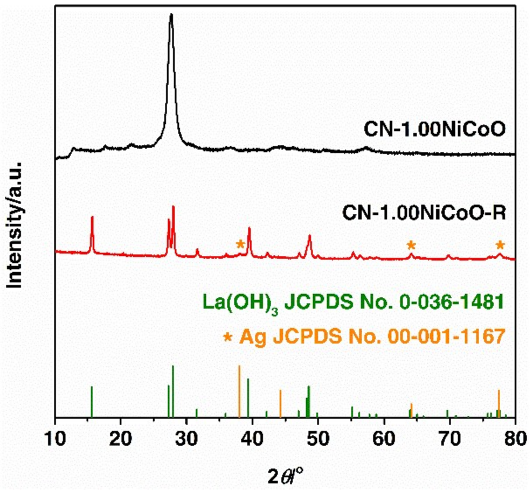

Figure S14. XRD patterns of CN-1.00NiCoO and CN-1.00NiCoO-R (obtained by recycling the photocatalyst after photocatalytic O_2-evolution reaction).

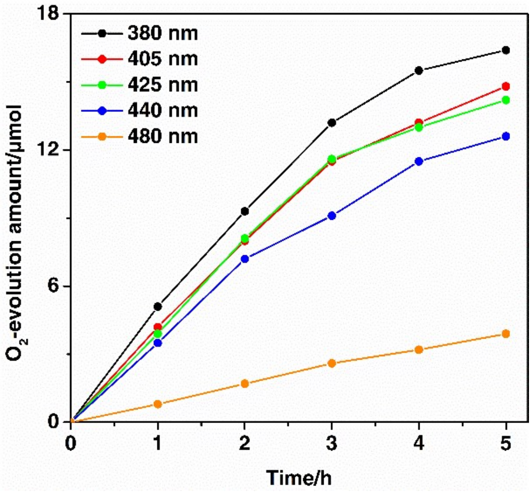

Figure S15. Time courses of photocatalytic O_2 evolution over CN-1.00NiCoO under different wavelengths (380, 405, 425, 440 and 480 nm).

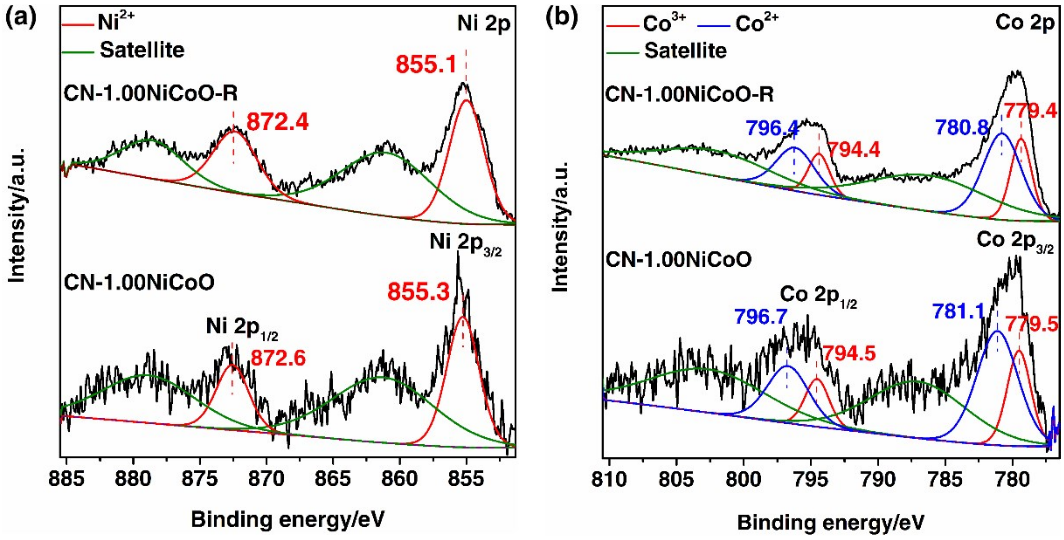

Figure S16. High-resolution XPS spectra of (a) Ni 2p and (b) Co 2p for CN-1.00NiCoO and CN-1.00NiCoO-R (obtained by recycling the photocatalyst after photocatalytic O_2 evolution reaction).

Table S1. Rates and quantum efficiencies of photocatalytic O_2 evolution over g-C_3N_4 modified with a series of cocatalysts. Sacrificial reactant solution: $AgNO_3$ aqueous solution (0.01 M).

Host photocatalyst	Cocatalyst	O_2-evolution rate /μmol h^{-1}	AQY/%	Reference
g-C_3N_4	**$NiCo_2O_4$**	**56.8 (full arc)**	**4.9 (380 nm)**	**This work**
Br doped g-C_3N_4	CoO_x	23.0 (full arc)	/	1
g-C_3N_4	$Co(OH)_2$	27.4 (full arc)	/	2
g-C_3N_4	$CoSe_2$	34.0 (full arc)	/	3
g-C_3N_4	NiCoP@NiCo-Pi	15.6 (full arc)	0.6 (420 nm)	4
Co doped g-C_3N_4	/	13.0 (full arc)	/	5
Boron-doped and nitrogen-deficient g-C_3N_4	$Co(OH)_2$	28.1 (full arc)	3.7 (380 nm)	6
g-C_3N_4	$CoMn_2O_4$	18.3 (full arc)	1.0 (380 nm)	7
g-C_3N_4	Co_3O_4	25.1 ($\lambda > 420$ nm)	1.1 (420 nm)	8

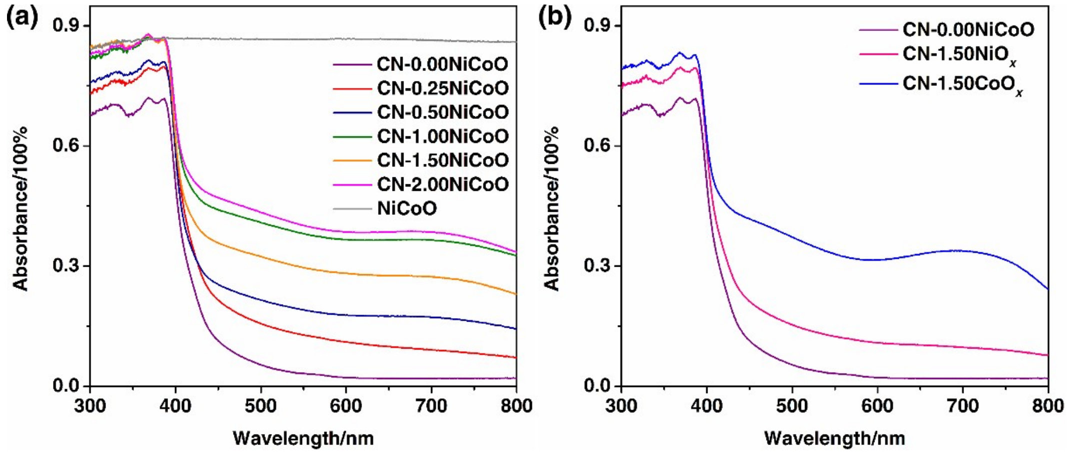

Figure S17. UV–vis spectra of (a) NiCoO, CN-*x*NiCoO (*x* = 0.00, 0.25, 0.50, 1.00, 1.50 and 2.00), and (b) CN-0.00NiCoO, CN-1.50NiO$_x$ and CN-1.50CoO$_x$.

The C−V measurements were performed for CN-0.00NiCoO and CN-1.00NiCoO in dark and under light irradiation, it showed that no redox peak derived from the faradaic reaction was detected for both samples no matter in dark or under light irradiation, water oxidation reaction occurred to produce oxygen, implying that CN-0.00NiCoO and CN-1.00NiCoO possessed good chemical stability. In addition, the current intensities of the C−V curves under light irradiation for both electrodes were higher than those in dark, respectively, implying that light irradiation could promote faster redox reaction kinetics.

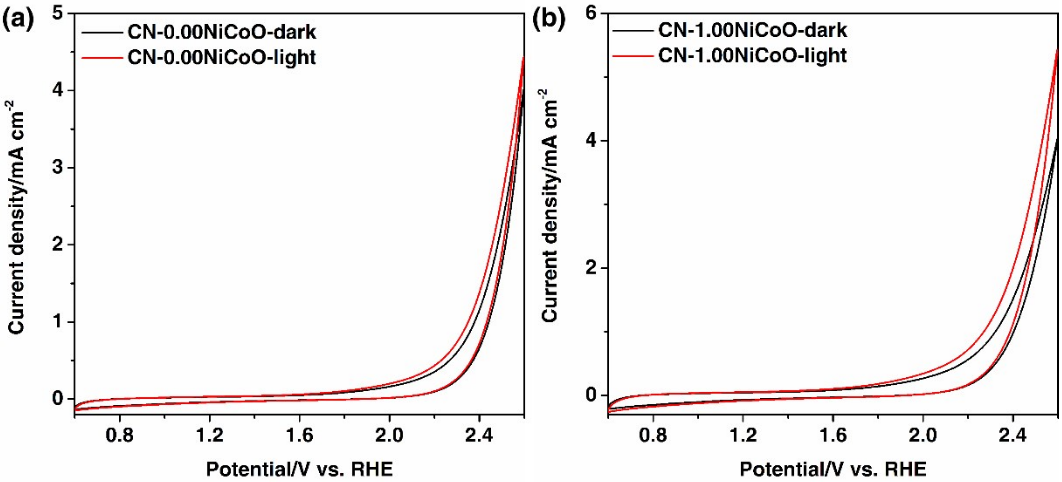

Figure S18. C−V curves for (a) CN-0.00NiCoO in dark (CN-0.00NiCoO-dark) or under light irradiation (CN-0.00NiCoO-light) and (b) CN-1.00NiCoO in dark (CN-1.00NiCoO-dark) or under light irradiation (CN-1.00NiCoO-light). Electrolyte: 0.5 M Na_2SO_4.

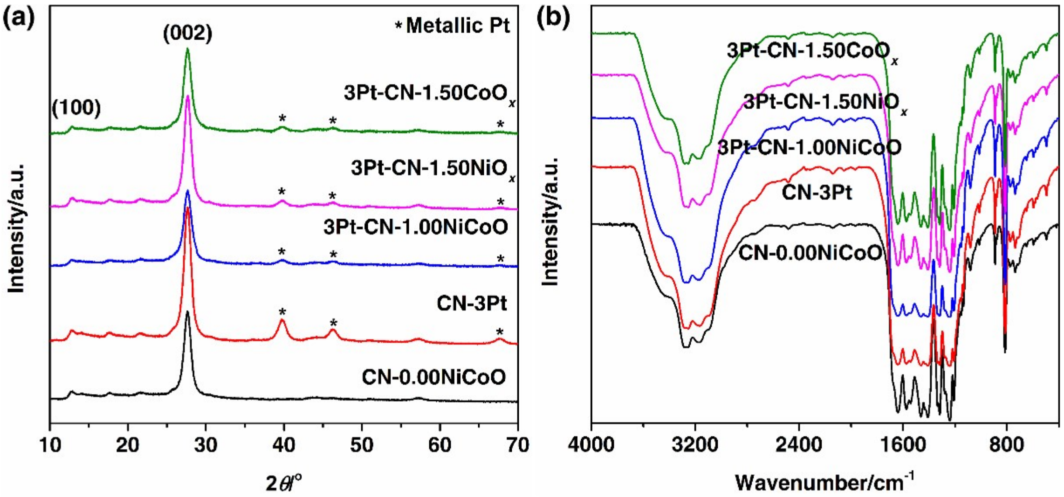

Figure S19. (a) XRD patterns and (b) FTIR spectra of CN-0.00NiCoO, CN-3Pt, 3Pt-CN-1.00NiCoO, 3Pt-CN-1.50NiO$_x$ and 3Pt-CN-1.50CoO$_x$.

It was noticed that CN-3Pt was prepared by photodeposition procedure in the presence of TEOA (10 vol%) as hole sacrificial agent in the reaction solution, because Pt was hardly photodeposited on CN in the pure water.

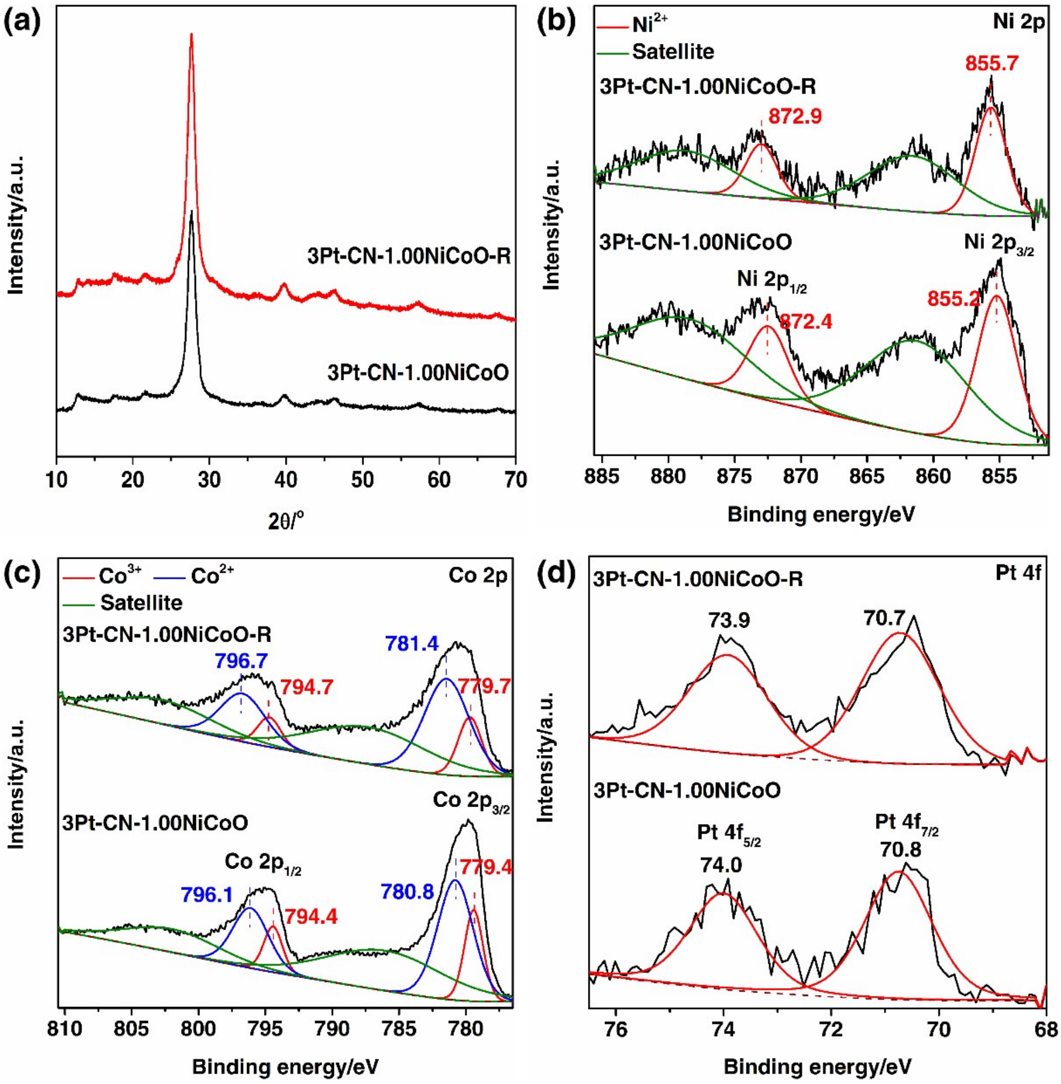

Figure S20. (a) XRD patterns, High-resolution XPS spectra of (b) Ni 2p, (c) Co 2p and (d) Pt 4f for 3Pt-CN-1.00NiCoO and 3Pt-CN-1.00NiCoO-R (obtained by recycling the photocatalyst after photocatalytic overall water splitting reaction).

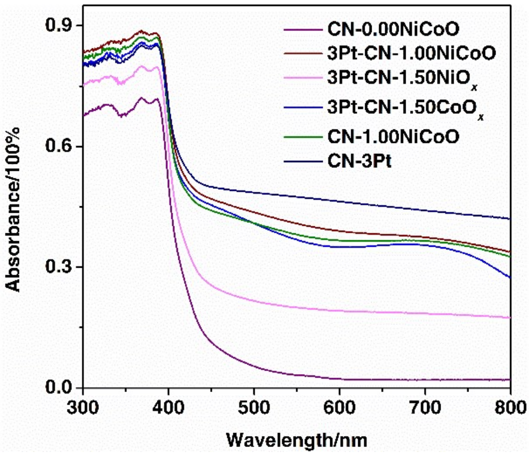

Figure S21. UV-vis spectra of CN-0.00NiCoO, 3Pt-CN-1.00NiCoO, 3Pt-CN-1.50NiO$_x$, 3Pt-CN-1.50CoO$_x$, CN-1.00NiCoO and CN-3Pt.

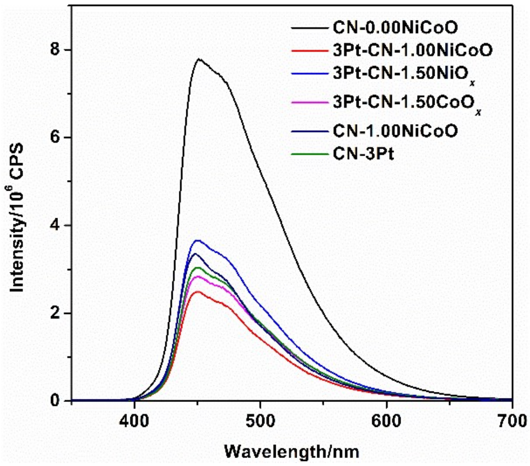

Figure S22. PL spectra of CN-0.00NiCoO, 3Pt-CN-1.00NiCoO, 3Pt-CN-1.50NiO$_x$, 3Pt-CN-1.50CoO$_x$, CN-1.00NiCoO and CN-3Pt.

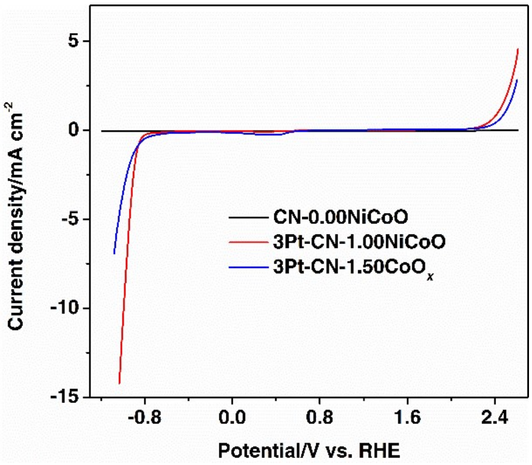

Figure S23. LSV curves for CN-0.00NiCoO, 3Pt-CN-1.00NiCoO and 3Pt-CN-1.50CoO$_x$. Electrolyte: 0.5 M Na_2SO_4.

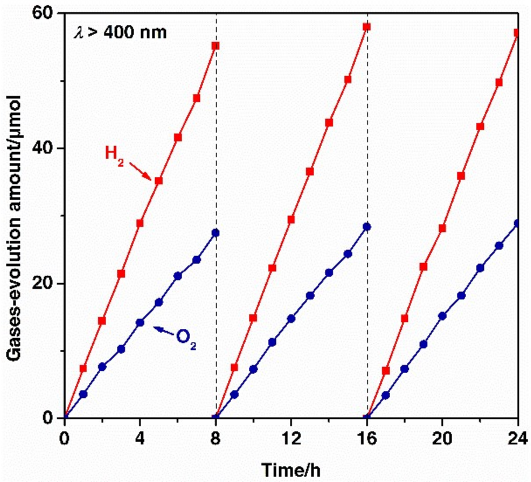

Figure S24. Time courses of H_2 and O_2 production for photocatalytic overall water splitting under visible-light irradiation ($\lambda > 400$ nm) over 3Pt-CN-1.00NiCoO.

Table S2. Rates and apparent quantum yields of photocatalytic overall water splitting over g-C_3N_4 modified with a series of cocatalysts.

Host photocatalyst	Cocatalyst	H_2/O_2 evolution rate /μmol h^{-1}	AQY/%	Reference
g-C_3N_4	**Pt, $NiCo_2O_4$**	**21.7/10.6 (full-arc)** **7.4/3.6 ($\lambda > 400$ nm)**	**2.8 (380 nm)**	**This work**
g-C_3N_4	Pt, PtO_x, CoO_x	12.2/6.3 (full-arc) 1.2/0.6 ($\lambda > 420$ nm)	0.3 (405 nm)	9
g-C_3N_4	Pt, CoP	2.1/1.0 (full-arc)	-	10
g-C_3N_4	Pt, Mn_3O_4	3.6/1.8 ($\lambda > 420$ nm)	-	11
phosphorus-doped g-C_3N_4 microrods	Pt, Ru	5.5/2.2 ($\lambda > 350$ nm)	-	12
phosphorus-doped g-C_3N_4	Co_xNi_yP	2.4/- ($\lambda > 420$ nm)	1.9 (380 nm)	13
PTI/Li^+Cl^- single crystals	Pt, Co	189.0/91.0 ($\lambda > 300$ nm)	8.0 (365 nm)	14

TEM and STEM for 3Pt-CN-1.00NiCoO-R shows cocatalysts were clearly anchored on the CN nanosheets, notable deviation in elemental scope and the scattered distribution for EDX elemental mapping images further indicated that Pt small nanoparticles and NiCoO decorated on the CN nanosheets with spatially separated positions.

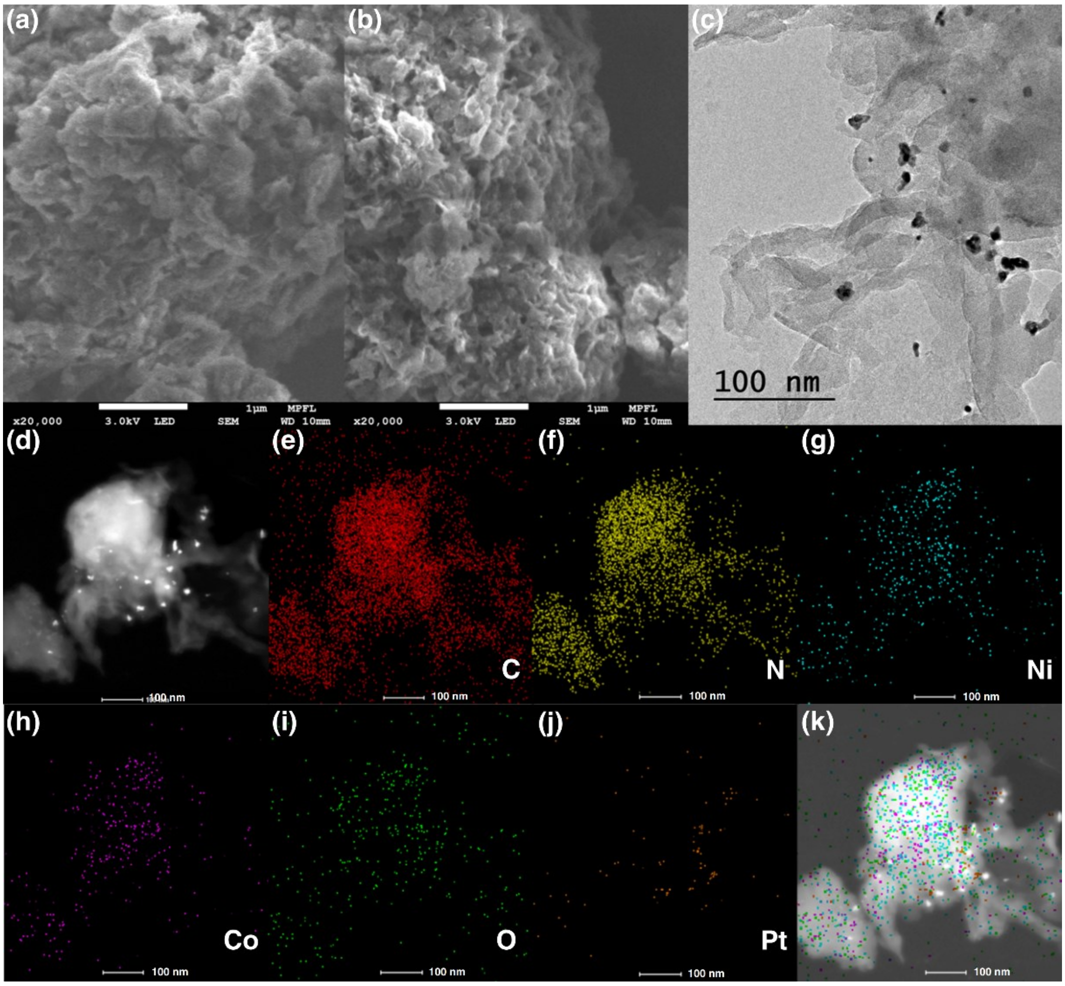

Figure S25. SEM images for (a) 3Pt-CN-1.00NiCoO and (b) 3Pt-CN-1.00NiCoO-R, the latter was obtained by recycling the photocatalyst after photocatalytic overall water splitting reaction. (c) TEM images for 3Pt-CN-1.00NiCoO-R, (d) STEM image and (e-j) EDX elemental mapping results of (e) C, (f) N, (g) Ni, (h) Co, (i) O, (j) Pt elements and (k) overlapping of Ni, Co, O and Pt elements for 3Pt-CN-1.00NiCoO-R.

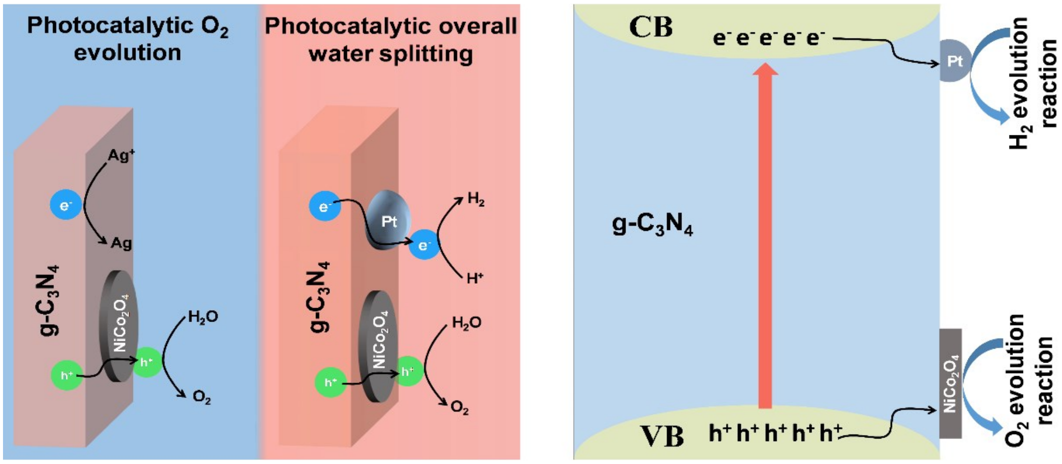

Figure S26. Schematic illustration of photocatalytic O_2 evolution on $NiCo_2O_4$/g-C_3N_4 and photocatalytic overall water splitting on (Pt,$NiCo_2O_4$)/g-C_3N_4.

References

[1] Z. Lan, G. Zhang and X. Wang, Appl. Catal. B Environ., 2016, **192,** 116−125.

[2] G. Zhang, S. Zang and X. Wang, ACS Catal., 2015, **5,** 941−947.

[3] G. Zhang, S. Zang, Z. Lan, C. Huang, G. Li and X. Wang, J. Mater. Chem. A, 2015, **3,** 17946−17950.

[4] Z. Qin, Y. Chen, Z. Huang, J. Su and L. Guo, J. Mater. Chem. A, 2017, **5,** 19025−19035.

[5] G. Zhang, C. Huang and X. Wang, Small, 2015, **11,** 1215−1221.

[6] D. Zhao, C. Dong, B. Wang, C. Chen, Y. Huang, Z. Diao, S. Li, L. Guo and S. Shen, Adv. Mater., 2019, **31,** 1903545−1903554.

[7] L. Zhang, C. Yang, Z. Xie and X. Wang, Appl. Catal. B Environ., 2018, **224,** 886−894.

[8] J. Zhang, M. Grzelczak, Y. Hou, K. Maeda, K. Domen, X. Fu, M. Antonietti and X. Wang, Chem. Sci., 2012, **3,** 443−446.

[9] G. Zhang, Z. Lan, L. Lin, S. Lin, X. Wang, Chem. Sci., 2016, **7**, 3062.

[10] Z. Pan, Y, Zheng, F. Guo, P. Niu, X. Wang, ChemSusChem., 2017, **10**, 87-90.

[11] Y. Li, S. Zhu, X. Kong, Y. Liang, Z. Li, S. Wu, C. Chang, S. Luo, Z. Cui, J. Colloid Interf. Sci., 2021, **586**, 778-784.

[12] L. Chen, X. Zhao, X. Duan, J. Zhang, Z. Ao, P. Li, S. Wang, Y. Wang, S. Cheng, H. Zhao, F. He, P. Dong, C. Zhao, S. Wang, H. Sun, ACS Sustain. Chem. Eng., 2020, **8**, 14386−14396.

[13] F. Xue, Y. Si, M. Wang, M. Liu, L. Guo, Nano Energy, 2019, **62**, 823-831.

[14] L. Lin, Z. Yin, J. Zhang, X. Cai, W. Lin, Z. Yu, X. Wang, Nat. Catal., 2020, **3**, 649-655.